Factors Controlling the Magnesium Weld Morphology in Deep Penetration Welding by a CO_2 Laser

M. Marya and G.R. Edwards

(Submitted 30 September 2000)

In laser welding with power density beyond 10^4 W · mm^{-2}, the formation of plasma cavities, commonly referred to as keyholes, leads to deep penetration welds with high aspect ratios. In this paper, the morphologies of keyhole welds produced with a 6 kW CW CO_2 laser on two die-cast magnesium alloys, AZ91 and AM50, are compared. It was found that the two magnesium alloys responded differently to laser welding. Though irregular weld cross-section profiles were consistently observed on each material, bead dimensions often varied with the welding variables in contrasting ways. For both alloys, important characteristics of the weld beads such as depth, width, crown height (hump), and surface ripples were analyzed as a function of the welding parameters, most particularly the heat input. Results show that the use of heat input, a variable grouping two welding parameters into one, was often inadequate in characterizing the bead morphology. Several explanations are given, including base metal vaporization, but the process of bremsstralung absorption explains it well and rationalizes many observed characteristics of laser weld morphology.

Keywords alloy AM50, alloy AZ91, CO_2 laser, magnesium alloys, welding

1. Introduction

In the last two decades, the manufacturing industry has been actively engaged in qualifying laser welding, because high strength joints with low levels of residual stress and high visual quality can be achieved with this joining process. The ability to achieve several operations with the same equipment (*i.e.*, cutting, drilling, surface treatments and even forming) also adds to these advantages. However, the expensive investment to acquire laser systems, together with high operating costs, has slowed their introduction into manufacturing. In recent years, the interest in magnesium and its alloys has grown significantly, because they have high specific strengths and can be recycled at competitive cost. The largest demand for magnesium alloys has come from the automotive industry, where the weight savings achieved by replacing steel and aluminum creates a major impact on reducing fuel consumption.

To date, published information on magnesium welding is still limited because magnesium has not been extensively utilized as a structural material. In the 1930s[1] the necessity to join magnesium alloys for aircraft components was partially at the origin of the gas tungsten arc welding process, and magnesium welding was reported in the early days of the gas tungsten arc welding (GTAW) process. Until recently, magnesium welding has been reported by only a few investigators.[2–6] The advantages offered by lasers and the current interest for magnesium have given incentive to the laser welding of magnesium. In the past few years, several papers have been published to primarily evaluate the full potential of lasers for joining magnesium components. Weisheit *et al.*[7] recently investigated the laser welding of several magnesium alloys, including AZ91 and AM50. Sanders *et al.*[8] studied the weldability of AZ31 thin sheets with both Nd:YAG and CO_2 lasers. Dilthey *et al.*[9] centered their study on the mechanical properties of magnesium joints produced by laser and electron beam welding. Marya *et al.*[10] looked at the variations of the local properties of weld beads in relation to the welding parameters. Although numerous studies relate weld bead morphology, process parameters, and heat flow, research to establish similar relationships at high power density[11–14] with magnesium alloys is still nonexistent.

This research addresses the weld bead morphology obtained after laser welding two die-cast magnesium alloys, AZ91 and AM50. A wide range of welding parameters was covered, but always with the perspective to produce keyhole welds, *i.e.*, welds with depth-to-width ratios typically greater than unity. Because deep penetration welds often exhibit complex shapes that require more than depth and width to fully characterize, other dimensions of the weld pools have been considered. The simple concept of heat input, as defined from the ratio of power with travel speed, was adopted in this study to investigate weld bead morphology changes. Weld bead morphology data of the two alloys are used to discuss the role of heat input. Because properties of the keyhole largely control the overall heat transfer, and therefore the weld pool morphology, they are first considered. To help establish relationships between keyhole properties and weld morphology, heat transfer by the process of bremsstralung absorption is first analyzed. Data related to the bead geometry of both alloys, AZ91 and AM50, are then compared and discussed based upon this background information and recently published information on deep penetration welding.

2. Theoretical Background

Early contributions with arc welding processes[15,16] have shown that it is often possible to rationalize weld bead morphologies from the thermal properties of the base material. In deep

M. Marya and **G.R. Edwards,** Center for Welding, Joining, and Coatings Research, The G.S. Ansell Department of Metallurgical and Materials Engineering, Colorado School of Mines, Golden, CO 80401-18887. Contact e-mail: mmarya@mines.edu.

penetration welding, the heat transfer is mainly affected by the properties of the plasma within the keyhole. Comparatively, the properties of the solid or liquid materials play a lesser role. An analysis of weld morphology thus requires knowledge of several properties of the keyhole.

The absorption of light and its conversion to heat is essentially an electronic process, by which electrons absorb photons, gain kinetic energy (in the form of vibration), and are promoted to higher energy states. In the crystal lattice, phonons also interact with the incoming photons from the laser beam, which causes phonon energy to increase and lifetime to decrease. Phonons cease to exist when the lattice periodicity breaks up and atoms free themselves from their neighbor interactions. Once melting and vaporization occur, the absorption is reduced to the electronic contribution. The absorption of energy continues to free electrons from their core ions, thus creating an ionized gas, referred to as plasma. Electrons absorb a significant part of the laser power by a process known as inverse bremsstrahlung absorption.[14,17] First, the absorption increases because the population of electrons having low energy increases. However, as their energy increases, interaction with the incoming photons also decreases. Ultimately, the electron energy exceeds that of the photon, causing photons to "rebound." As a result, absorption eventually decreases, thus meaning that the plasma becomes more transparent. This process of inverse bremsstrahlung absorption[14,17] can be quantified as

$$a_w = \frac{n_e n_i e^6 \left[1 - \exp\left(-\frac{h\omega}{2\pi k T_e}\right)\right]}{6\sqrt{3}\mu\varepsilon_0^3 c\left(\frac{h}{2\pi}\right)\omega^3 m_e^2}\left(\frac{m_e}{2\pi k T_e}\right)^{1/2}\bar{g} \qquad \text{(Eq 1)}$$

where n_e and n_i are the ion and electron density, respectively; e is the electron charge; h is the Planck's constant; ω is the angular frequency of the laser radiation ($1.7 \cdot 10^{14}$ Hz for a CO_2 laser); k is the Boltzmann's constant; T_e is the electron temperature; μ^2 is the real part of the refraction index (approximately unity); and g is the average Gaunt factor, which for a CO_2 laser is well approximated by[18]

$$\bar{g}_{co_2} = \left(\frac{T_e}{2116\ \text{K}}\right)^{0.227} \qquad \text{(Eq 2)}$$

Important variables that affect the properties of the keyhole are the electron and ion densities as well as the temperature. Assuming an equilibrium state, electron and ion densities can be computed as a function of temperature by using Saha's equation, which has been used by numerous investigators.[14,17,18] Like a chemical equation for a reaction, densities (concentrations) of each species can be related to a temperature-dependent quantity, conventionally referred to as the equilibrium constant. A simplified form of Saha's equation is the following:

$$\frac{n_e n_{Z+1}}{n_Z} = 2\left(\frac{2\pi m_e}{h^2}\right)^{3/2}(kT_e)^{3/2}\exp\left(\frac{-E_i}{kT_e}\right) \qquad \text{(Eq 3)}$$

where n_Z is the density of species with charge $+Z$ (their sum equals the ion density), and E_i is the ionization potential. First and second ionization potentials are provided in Table 1 with other important properties of either the elements or the alloys of this study.

Although few experimental measurements of temperatures within the keyhole exist, spectroscopic measurements first published indicated that the plasma temperature was about 6800 K.[19] Arata *et al.*[20] experimentally demonstrated that it was greater than 5500 K. Metzbower[14,21] used a thermodynamic model to show that the keyhole temperatures could be far greater. Tix and Simon[17] demonstrated by solving a set of transport equations that the keyhole temperature could be as high as 19,000 K. Electron-ion densities of $4 \cdot 10^{23}$ m^{-3} were also found, with degrees of ionization ranging from 90% in the hottest plasma to 10% near the keyhole wall. Regardless of the exact temperature, all these results suggest that the second ionization is unlikely. Saha's equation hence can be simplified, considering only the first ionization. Specie densities thus involved are the initial atom density, n_0, and the ion-electron densities, which equal each other because of charge neutrality. The degree of ionization, α, defined in Eq 4, varies between zero and unity, a value reached for an entirely ionized population of initially neutral atoms. The degree of ionization provides information concerning the composition of the plasma and is estimated using Saha's equation (given as Eq 3) and the following relationship:

$$\alpha^2 = \left(\frac{n_e n_i}{n_0}\right)\left(1 + \frac{n_e n_i}{n_0}\right)^{-1} \qquad \text{(Eq 4)}$$

Figure 1 shows the variations of the degree of ionization as a function of temperature for various species present in both materials. It can be seen that aluminum is the first element to lose an electron due to its lower ionization potential. On the other hand, zinc, the first element to vaporize, requires a greater energy to release its first electron. Equation 1 shows that the bremsstrahlung absorption coefficient is directly proportional to the product of electron-ion densities, which can be rearranged to be expressed as a function of the degree of ionization and the initial atom density (Eq 4). For simplification, absorption coefficients were normalized with respect to the maximum value calculated for aluminum (aluminum generates the most absorbing plasma). The interaction between a CO_2 laser and various pure metal plasmas is summarized in Fig. 2.

3. Experimental Procedure

Bead-on-plate experiments were made with a 6 kW CW CO_2 laser on two commercially available magnesium alloys: AM50, an alloy containing 5 wt.% aluminum and 0.5 wt.% manganese; and AZ91, an alloy with 9 wt.% aluminum and 1 wt.% zinc. All 100 × 80 × 8 mm test specimens were cut from die-cast materials. As a result of machining, the surface finish of all specimens was identical. Prior to welding, the test specimens were cleaned with ethanol. Up to eight weld beads (depending upon the resulting weld width) were produced on

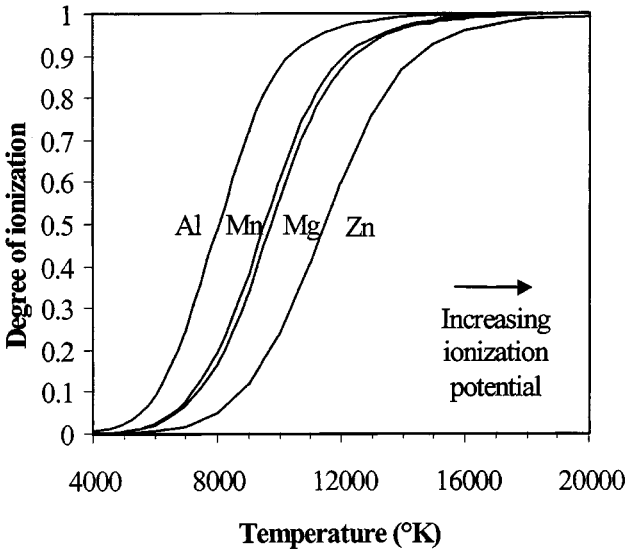

Fig. 1 The degree of ionization as a function of temperature for a number of elements

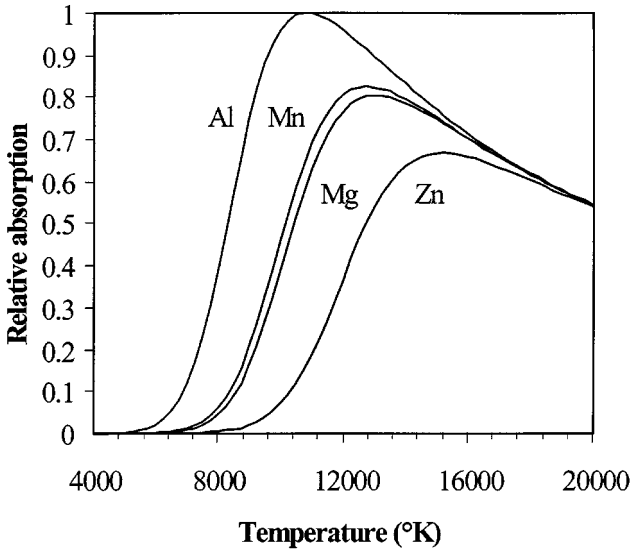

Fig. 2 The bremsstrahlung absorption as a function of temperature

Table 1 Important physical properties of the elements found in the AM50 and AZ91 magnesium alloys[25]

	Mg	Al	Zn	Mn	He	AM50	AZ91
Melting point (K)	922	933	693	1517	…	615 °C	596 °C
Boiling point (K)	1363	2793	1180	2335	…	…	…
First ionization potential (eV)	7.646	5.986	9.394	7.435	24.857	…	…
Second ionization potential (eV)	15.061	18.861	17.995	15.666	…	…	…

each specimen. The spacing between each weld was approximately 10 to 15 mm.

All the beads were fabricated with the beam precisely focused onto the specimen surface. The beam diameter, estimated from earlier beam profile analyses, was approximately 0.5 mm. During welding, helium was used as a shielding gas because of its higher ionization potential. The main shielding was provided by a nozzle assembly coaxially fixed on the laser head. The gas flow rate was 30 L · min^{-1} in all trials. The back surface of the specimens, also exposed to the surrounding air, was protected by a secondary helium flow. Specimens were clamped from the side and held approximately 10 mm above a graphite-coated plate, placed there to stop possible excess power of the beam. All welding experiments were conducted with a constant beam diameter. As a result, the primary independent variables were reduced to the beam power, the beam speed, and the material. The beam power and the beam speed were varied between 2000 and 5000 W and 500 and 6000 mm · min^{-1}, respectively.

Prior to cross sectioning, weld bead surfaces were photographed so that discontinuities such as cuts, undercuts, crowns, or irregular ripples could be analyzed together with the bead morphology. Once cut, the samples were prepared for standard optical metallography. Cross sections were examined to quantify major characteristics of the weld bead morphology. The bead profile was revealed after a short nital etching.

4. Experimental Results

In autogeneous welding, two characteristics of the weld cross section are usually considered. They are the depth and the width of the fusion zone. At low power density, the entire weld profile can often be described with only these two dimensions. In deep penetration welding of magnesium, the keyhole gives rise to large variations in weld width across the thickness, as depicted in Fig. 3. The bead profile often resembles a nail because the upper section is broader and circular while the remaining fusion zone is significantly narrower. For convenience, this narrow and elongated part of the weld will be referred to as the weld column. Protrusions of the fusion boundary into the base metal could also be observed in this weld column, especially when the power density was increased beyond that required to reach complete penetration. These deformities suggest that both the fusion boundary and keyhole could have oscillated extensively, as detailed by Kroos *et al.*[22] and Klein *et al.*[23] A single protrusion was usually present within the weld column. It was found to grow from the back of the plate and to move upward as the power density increased. These local deformities were not measured, but they are subject to discussion later in this paper.

Once the weld geometry is defined by quantifiable parameters, it can be studied as a function of several combinations of single variables. It is usually convenient to group beam power

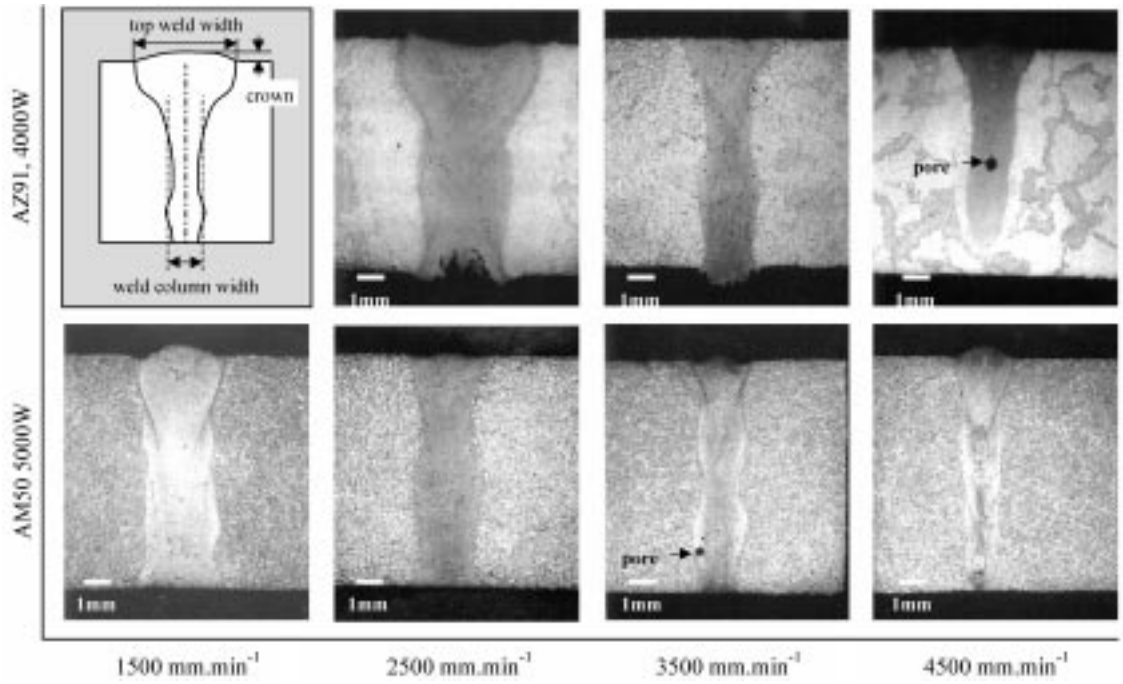

Fig. 3 Cross-section macrographs of laser beam welds produced in AM50 and AZ91 alloys

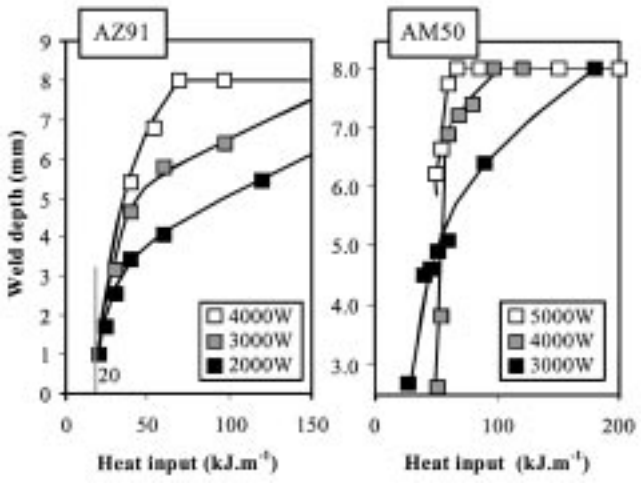

Fig. 4 The effect of the heat input on the weld depth for the AZ91 and the AM50 alloys

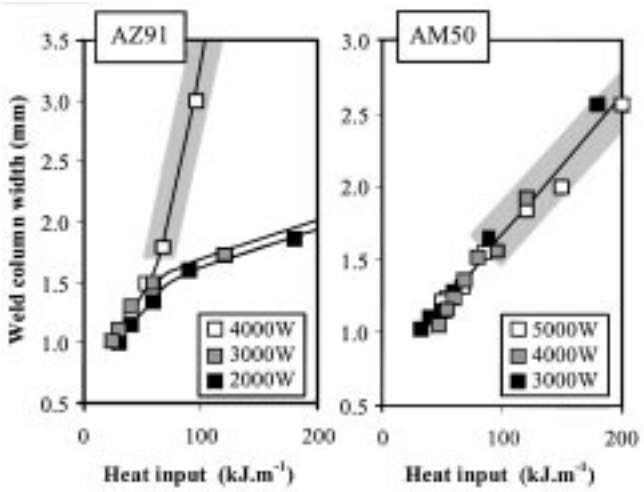

Fig. 5 The effect of the heat input on the width of the weld column for the AZ91 and the AM50 alloys

and beam speed into one parameter, the heat input, defined as the ratio of the beam power to the beam travel speed. In this study, experimental data were represented as a function of the heat input. Weld morphology data, on cross sections and at the surface, are consecutively presented.

4.1 Weld Bead Cross-Section Dimensions

Figure 4 to 7 depict various weld characteristics as a function of the heat input. Complete weld bead penetration is indicated by the shaded areas.

When these data are taken as a whole, several trends can be observed. The most striking feature is the incomplete dependence upon the heat input. Each weld characteristic remained a function of the beam power after being plotted against the heat input. Consequently, there was no advantage in regrouping beam speed and beam power, because an entire description of the bead geometry still required two variables. However, most quantities tended to converge toward similar finite values when plotted versus the heat input. As shown in Fig. 4 for the AZ91 alloy, the minimum heat input for keyhole welding was approximately 20 kJ $\cdot$ m^{-1}. The power density, derived at 5500 mm $\cdot$ min^{-1}, was then approximately 10^4 W $\cdot$ mm^2. In the AM50 alloy, a similar heat input for keyhole welding can be extrapolated.

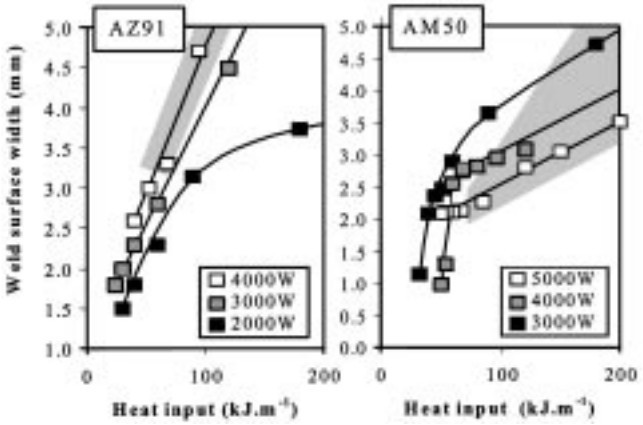

Fig. 6 The effect of the heat input on the weld surface width for the AZ91 and the AM50 alloys

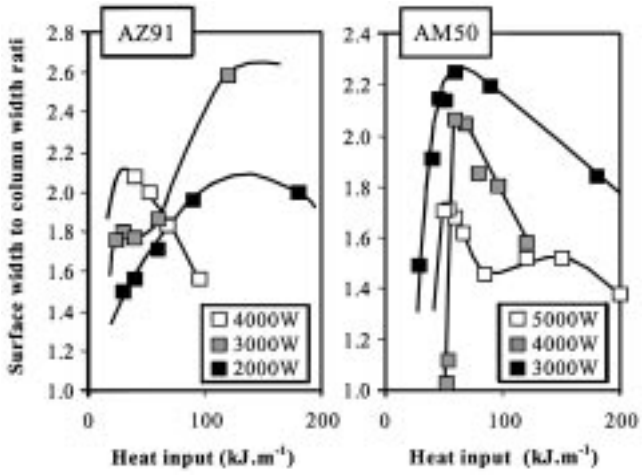

Fig. 7 The effect of the heat input on the weld aspect ratio

However, a number of data repeatedly showed that the AM50 alloy responded quite differently to laser welding.

When the heat input is taken as a constant and each material considered individually, other features can be emphasized. In the AZ91 alloy, Fig. 4 and 6 show that high beam powers led to deep and wide beads. However, the quasi-proportional increase in weld depth seen between 40 and 100 kJ · m^{-1} in the AZ91 alloy (Fig. 4) was not encountered for the width of the weld column (Fig. 5). While depth increased quite uniformly, a slight increase in the weld column width was first observed when the power was raised from 2000 to 3000 W. The width of the weld column then increased rapidly with further beam power, as observed at 4000 W. It thus appears that both weld depth and surface width increased before the weld column widened.

In the AM50 alloy, results suggest a different interpretation. First, the weld depths measured at 3000 W were repeatedly greater than those at 4000 W at the lowest heat inputs. Although an increase in beam power normally enlarges the dimensions of the fusion zone, as shown in the AZ91 alloy for both the width of weld column (Fig. 5) and the width of the weld at the

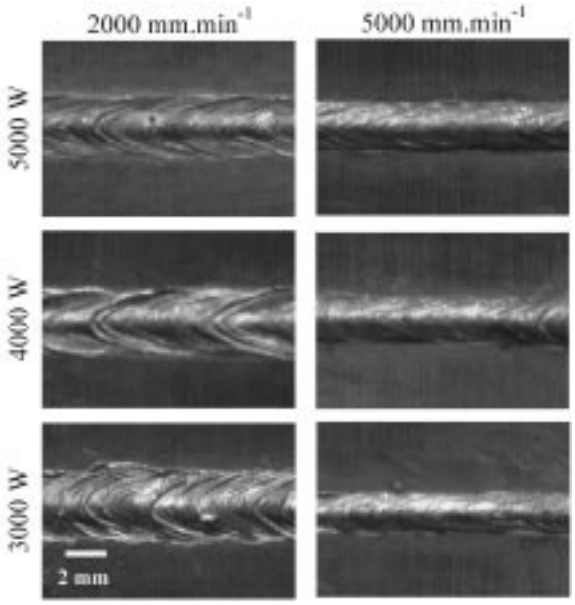

Fig. 8 The weld surface patterns of AM50 welds produced under various combinations of beam power and beam speed

surface (Fig. 6), the weld widths in the AM50 alloy followed different trends. The width of the weld column was not observed to vary, which implies that the heat input consistently determined this characteristic. Perhaps the greatest difference between the two materials is shown in Fig. 6, where variations of the weld width at the surface are plotted against the heat input. For the most part, weld surface width also varied proportionally with the heat input, except at low heat input.

In Fig. 7, the ratio of the weld surface width to the column width is shown as a function of the heat input. This aspect ratio was found to pass through a maximum when the heat input was varied. While these maxima occurred at almost identical heat inputs in the AM50 material, confirmation was not found in the AZ91 alloy. Furthermore, the position of these maxima could not be correlated to either the heat input or the beam power. Nevertheless, aspect ratio maxima were consistently found when the weld depth was between 5 and 7 mm (between 60 and 85% of the plate thickness).

4.2 Weld Bead Surface Topography

The effects of the process parameters on the geometry of the bead surface are depicted in Fig. 8 for the AM50 alloy only. At the lowest beam speeds, the bead surface displayed a marked chevronlike pattern or ripples. At higher speeds and regardless of the beam power, these surface ripples had a tendency to disappear. Ripples were also strongly elongated and in greater density, which explains why they were more difficult to differentiate. At the highest beam powers, ripples were considerably smaller than at low power, which suggests that high powers also reduce surface ripples. These few results demonstrate that ripples are not controlled solely by the heat input, because both beam power and beam travel speed reduce ripples.

Furthermore, it has been observed that the welds produced at high welding speeds were generally slightly elevated above

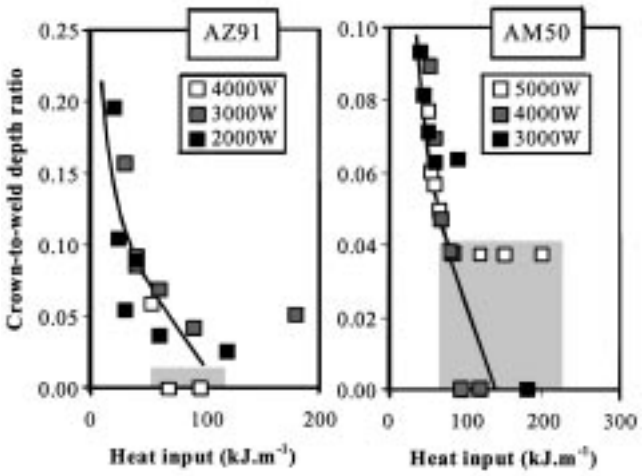

Fig. 9 The effect of the heat input on the magnitude of the weld crown relative to the weld depth

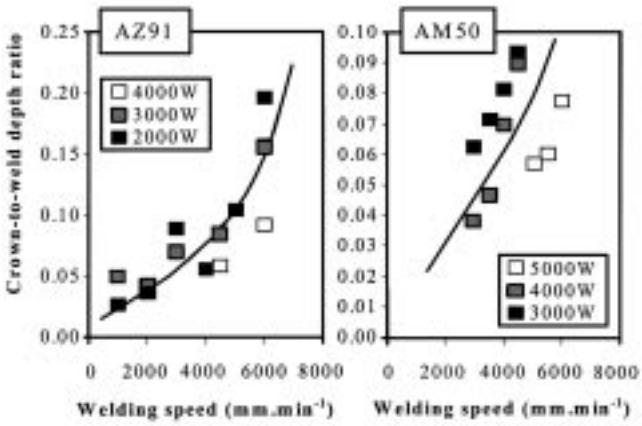

Fig. 10 The effects of the beam speed and the beam power on the magnitude of the weld crown relative to the weld depth

the surface. Figure 9 shows that this elevation or crowning (also sometimes called humping), represented by another aspect ratio (the crown-to-weld depth ratio), was controlled by the heat input, and consistently increased with decreasing heat inputs. At the largest welding speeds, discontinuities in the weld surface pattern appeared. High crowns followed by deep surface depressions were periodically observed along the bead. Although there was, on average, no change of height, these periodic variations in topography were not found at other welding speeds, where the heat input was identical. Clearly, beam speed and beam power cause different degrees of crowning.

The effects of both the beam power and the beam speed are illustrated in Fig. 10 for partial penetration welds only. It was found that, when their combination was such that the heat input was above the minimal heat input for complete penetration, the weld typically collapsed. Severe undercutting resulted on the upper side of the welds, while the molten bead passed through the entire thickness on the other side. This led to a very irregular weld defect on the plate backside, which has often been referred to as "cutting." Since full penetration welds were not subject to crowning, Fig. 10 did not include such welds. Figure 10 shows that crowning was primarily influenced by the welding speed. Crowning increased strongly with the welding speed and decreased with the beam power. Under similar welding conditions, crowning was significantly greater in the AZ91 alloy.

5. Discussion

5.1 Role and Significance of the Heat Input

The fact that the heat input, simply represented by the ratio of the beam power to the beam travel speed, was inadequate must be considered. At constant heat input, weld morphology data demonstrated that different combinations of beam power and beam speed led to different results. When both beam power and travel speed were low, melting was not attained because the laser beam was simply reflected. With the same heat input and greater values of both parameters, melting was achieved. With even larger beam power and travel speed, welding through a keyhole was made possible. In each of these situations, the process and efficiency at which the beam energy was converted to heat and transferred within the material was changed. Heat transfers within solid, liquid, or gaseous phases are quite different. Moreover, they are all modeled by nonlinear relations because they involve temperature-dependent properties. Under particular conditions, such as heat conduction, no exchange with the surrounding, constant physical properties, and either thick or thin plates, the heat flow is mathematically known to be proportional to the heat input.[11–13,15–16] In reality, physical properties vary with the temperature and the heat flow is nonlinear, which makes the use of a simple heat input rigorously inappropriate.

The heat flow is particularly nonlinear in weld pools where convection is dominant; *i.e.*, for high Peclet numbers.[24] Experimental evidence comes from infrared sensing measurements, which showed that weld pool temperatures do not increase proportionally with either the power or the reciprocal of the welding speed. In keyhole welding, the plasma also accentuates this nonlinearity with the heat input for various reasons. The problem of evaporation loss, well known to occur in laser welding of other alloys,[25,26] and the formation of an undesirable vapor fume shielding the weld pool could reduce the total heat input to the base material. Although significant power loss by this mechanism has not yet been completely verified, the transfer of the beam energy to the keyhole occurred predominantly by the process of bremsstrahlung absorption, a strongly nonlinear phenomenon with regard to temperature.

5.2 Alloying Effects and Heat Absorption

Figure 4 to 7 reveal very large differences in the bead profiles of both alloys. When the heat input was taken as a constant and the AZ91 alloy considered, increasing both the beam power and the beam speed widened the weld column and the weld at the surface. The fact that these two characteristics, in addition to the weld depth, increased with combinations of high beam power and high beam speed showed that the heat transfer was strongly nonlinear and increased with large parameters. In the

AM50 alloy, different trends were observed with the same consideration of constant heat input. For instance, the width of the weld column did not vary with increasing beam power, which might infer that the heat absorbed near the surface was roughly constant, regardless of the combination of beam power and beam speed. Like the AZ91 alloy, the weld depth increased with combinations of high beam power and high beam speed. However, under the same conditions, the column width shrank. The results on the weld depth imply that the heat transfer through the thickness consistently increased with combinations of high beam power and high beam speed. However, the results on the widths strongly suggest that the heat transfer lateral to the weld bead decreased. Figure 6 reports that decreasing widths were observed with melt-through beads. This important piece of information must be considered, because it suggests that large fractions of the incident beam power passed through the thickness, and thus reduced the overall heat input to the weld. This situation develops if the plasma absorption had already reached the point where it began to decrease. Figure 2, calculated from Eq 1 to 4, reveals that the plasma temperature had to exceed a temperature close to 10,000 K, a value consistent with that predicted by other research.[14,20,23–24]

These explanations carry several important consequences. First, decreasing widths with enhanced beam power should be expected if beam powers larger than those of this study had been used on the AZ91 alloy. Second, these experimental results also suggest that beam energy was more efficiently used in the welding of the AM50 alloy than in the AZ91 alloy. Complete penetration indeed occurred at lower heat input on the AM50 alloy. Figure 2 suggests that the AZ91 alloy with its greater aluminum content should more efficiently absorb the beam. However, these results, together with the compositional difference of the two alloys, raise the possibility of zinc vaporization, which could have reduced the overall beam absorption. Also, these results imply that the upper part of the weld enlarged more than the remaining portion of the bead for all conditions where the surface absorption increased with the heat input. Figure 2 predicts that keyhole absorption increased as long as the temperature remained below 10,000 K. When this situation is encountered, the surface width is predicted to increase with the beam power, which gives rise to the nail shape, also seen by Metzbower.[14] Careful examination of the data on the AM50 also confirmed these expectations. At 2000 and 3000 W, the column widths were similar, but considerably enhanced at 4000 W. As beam power increased further and caused higher plasma temperatures, the surface absorption eventually decreased. Eventually, more heat was transmitted into the bulk of the weld metal than into its surface, which caused the nail shape to fade. With the heat input excessively too high, a large part of the beam power simply passed through the thickness.

5.3 Transition between Two-Dimensional and Three-Dimensional Heat Flow

Although heat absorption (by the bremsstralung process) significantly affects weld bead morphology, it does not provide a complete explanation. For instance, some of the weld cross sections exhibited wavy profiles that are not fully explained by absorption. Figure 5 shows that the width of the weld surface attained a maximum relative to the column width for bead penetrations of approximately two-thirds the plate thickness. In the AM50 alloy, this feature developed at nearly constant heat input, which suggests that the dominant factor might be the welding speed. The fact that the widest weld surface was observed at two-thirds the plate thickness could be explained by heat conduction. It is known that the plate backside influences the heat flow when the weld depth approximates two-thirds of the plate thickness.[27] The back "reflection" of the incoming heat flux on the back surface causes the heat flow to gradually transform from three-dimensional to two-dimensional. Once two-thirds of the thickness is approximately reached, complete penetration rapidly occurs and the back weld width increases far more than the upper weld width.[28] The weld width thus culminates relative to the weld width on the backside when complete penetration begins, and then decreases. The situation is analogous, except that complete penetration was not reached. It is consequently difficult to verify that the maximum weld surface width-to-column width ratios occurred as a result of a change in heat flow, especially with laser welds where heat flows are predominantly two-dimensional.

The concept of a back reflection of a heat flux onto a surface can be developed further, especially considering the carbon-coated plate placed behind the welding specimens. When complete penetration occurred, a fraction of the laser radiation passed through the material. Although small, a fraction of this power was reflected back into the weld pool, and could thus explain why the weld pool enlarged noticeably from the backside.

5.4 Keyhole Stability and Weld Bead Cross-Section Deformities

Clearly, explanations other than absorption are required to fully understand current data. The cross-sectional macrographs of Fig. 3 demonstrate that the weld bead profile changed rapidly as the fusion boundary penetrated through the plate thickness. It is seen that the weld pool exhibited a wavy profile, which is partially explained by absorption but also affected by keyhole dynamics. It is well known that deep keyholes are naturally unstable, because the surface tension forces that laterally hold the molten metal must balance greater hydrostatic pressures as the depth of the pool increases. Eventually, the keyhole is predicted to collapse, as analyzed by Kroos *et al.*[22] Figure 3 tends to confirm that these oscillations could be particularly dominant once complete penetration was reached.

An estimate of a critical condition for keyhole instability can be made with a few assumptions. If hydrostatic equilibrium at the wall of a cylindrical keyhole of radius R is assumed, a simple relationship involving keyhole internal pressure P_i with γ, the surface tension, and ρgh, the liquid pool hydrostatic pressure, can be derived where h is the depth below the surface. Furthermore, when variations in density between liquid and keyhole plasma are neglected and the keyhole pressure P_i is rewritten as ρgH, where H is an equivalent height, it can be shown that the liquid column will no longer be stable when the parameter (H-h), a characteristic of the keyhole, exceeds the quantity $\gamma/(\rho gR)$. Based upon this simple model, the keyhole stability is found to increase with the surface tension and decrease rapidly with the inverse of the beam radius. Incorporating values for liquid magnesium, $\gamma = 0.57\ \mathrm{N \cdot m^{-1}}$, $\rho = 1700$

$kg \cdot m^{-3}$, and the beam radius as an estimate of the keyhole radius ($R = 1.7$ mm), one will find that (H-h) is approximately 20 mm. Physical properties were considered at the melting temperature. However, the surface tension should have been estimated at a higher temperature near the vaporization point (certainly, it cannot be taken at the vaporization point because it is then zero). In the absence of more suitable data, one can only anticipate that the actual critical depth will be much smaller than that predicted.

The estimated critical depth for the instability is 4 times greater than the measured value. Recall that the instability was typically observed at a depth of 5 mm if one considers that it coincides with a maximum (surface width)-to-(column width) ratio. It was postulated that such a significant change in geometry could be associated with optimal surface absorption. In regions of enhanced absorption, the keyhole diameter is expected to be widest, which decreases the critical depth, as explained earlier. It is thus not surprising to find protrusions of the fusion boundary after the surface width had reached a maximum relative to the column width. With larger beam powers, the depths of both the fusion boundary and the keyhole increased, and so did the instability and the protrusions. In their presence, it appears that the heat and mass exchange with the upper part of the pool will be reduced, thus promoting increased melting near the bottom of the keyhole. This might be confirmed by other observations. It was found that large pores tended to develop soon after the midthickness; *i.e.*, where the instability presumably developed. The fact that keyhole instability could promote porosity has been confirmed by several authors.[29–31]

With beam powers in excess of that for complete penetration, deformities along the fusion boundary were apparently reduced. At very high power density, as produced on the AM50 alloy, the widths of the weld pool decreased. This can be substantiated by Fig. 2, which shows that absorption eventually decreased. Due to reduced absorption, a small and more intense keyhole can be predicted. The fact that the keyhole diameter is smaller reinforces the point that its stability can be related to its diameter. With narrower keyholes, the stability of the melt column increases. Also, the porosity did disappear.

5.5 Crowning and Ripple Phenomena

It may be questioned whether crowning, ripples, and weld cross-section morphology can be related. Figure 8 to 10 showed a number of interesting features. High beam powers were found to reduce both ripples and crowning. High welding speeds also reduced ripples, but greatly increased crowning. It is clear that these two phenomena are independent. Furthermore, judging from Fig. 4 to 7 and 9, it appears that weld surface characteristics such as ripple and crowning and bead cross-section morphology can hardly be related.

The mechanism of ripple formation has been explained by D'Annessa.[;32] This phenomenon has been associated with growth rate fluctuations by considering the effects of surface tension of the weld pool during solidification. However, the less studied crowning phenomenon was considered in greater depth in this study. Figure 10 shows the crown increased rapidly with the welding speed. The effect of the beam power, although less important, was to increase crowning at lower beam power. When crowning occurred, the molten metal was essentially projected toward the rear of the weld pool. High travel speed increased the fluid flow in that direction. Crowning is consequently a pure hydrodynamic effect, as recently shown by Gratzke *et al.*[33]

The fact that crowning was approximately 3 times larger in the AZ91 than in the AM50 can be rationalized from the previous explanation. At fixed beam speed, enhanced crowning can be explained as a result of a decreased heat transfer due to zinc vaporization. This observation substantiates previous data for the width of the weld column.

In the presence of crowning, the constancy of matter (neglecting evaporation) requires the formation of voids or pores within the weld metal. However, due to the high welding speed and solidification rate, none of the critical events (nucleation, growth, and transport of large pores) had time to significantly develop, as shown by the optical macrographs presented in Fig. 3. Although microporosity was observed at greater magnification, the rare large pores encountered on a few welds appear to be related to enhanced keyhole instability.

6. Summary and Conclusions

This preliminary study on the deep penetration welding of magnesium alloys revealed interesting results. A number of questions, which arise from these experimental data, have been answered. Others questions, however, remain unanswered and require detailed analyses. However, the following conclusions have been reached.

- The useful concept of heat input, which groups two welding parameters into one, was not adequate in characterizing the keyhole welding of magnesium alloys. Several explanations have been given, but the process of bremsstrahlung absorption explains it best.
- The simple model of absorption, which was introduced in Section 2, provides explanations of many variations found in the weld bead morphology of both alloys. For instance, the nail head profile often encountered in laser welds could be seen as the result of enhanced surface absorption. With higher temperatures, surface absorption eventually decreased, thus giving rise to enhanced absorption within the bulk of the weld. Protrusions of the fusion boundary into the base material have been partially explained by this mechanism.
- The absorption model demonstrates that the condition of decreased absorption at high beam power requires keyhole temperatures greater than 10,000 K.
- It is probable that protrusions are not entirely caused by enhanced absorption. As the keyholes and weld pool get deeper, they become naturally unstable. Recall that keyhole instability decreases with larger diameter. As a protrusion developed below the surface, less surface absorption occurred but more absorption in the vicinity of this protrusion resulted. The keyhole thus widened where absorption was greatest and shrank where absorption decreased. As a result, enhanced instability within the keyhole is predicted to create welds with wavy cross-section profiles for these conditions.

- When comparing the welding of AZ91 and AM50 under similar conditions, significant differences have been found. For instance, greater weld penetration can be reached in the AM50 alloy. The explanation for this phenomenon is unclear, but it seems that zinc vaporization in the AZ91 could contribute to reduced heat.
- The phenomenon of crowning was found to be primarily dependent upon the welding speed. Large welding speed and low beam powers promoted crowning. Surface geometry of the welds was not related to weld cross-section profiles.

Acknowledgments

The authors thank Visteon Automotive System (Dearborn, MI) for funding this research. They also acknowledge Professor S.K. Marya, Ecole Centrale Nantes (Nantes, France), for the use of a CO_2 laser welding unit, and Dr. G. Kohn, Rotem Industries (Israel), for providing the magnesium used in this study.

References

1. *The Procedure Handbook of Arc Welding*, The Lincoln Electric Company, Cleveland, OH, 1995, pp. 1.1-1-1.1-10.
2. P. Klain: *Welding J.*, 1957, vol. 36 (7), pp. 321s-329s.
3. L.F. Lockwood:, *Welding J.*, 1965, vol. 44 (5), pp. 213s-220s.
4. L.F. Lockwood: *Welding J.*, 1970, vol. 49 (6), pp. 464-75.
5. H. Wohlfahrt and S. Juttner: in *Proc. Conf. on Magnesium Alloys and Their Applications*, Apr. 28-30, 1998, Werkstoff-Informationsgesellschaft mbH, Wolsburg, Germany, 1998, pp. 589-94.
6. A. Stern and A. Munitz: *J. Mater. Sci. Lett.*, 1999, vol. 18 (11), pp. 853-55.
7. A. Weisheit, R. Galun, and B.L. Mordike: *Welding J.*, 1998, vol. 77 (4), pp. 149s-154s.
8. P.G. Sanders, S. Keske, K.H. Leong, and G. Kornecki: *J. Laser Appl.*, 1999, vol. 11 (2), pp. 96-102.
9. U. Dilthey, H. Haferkamp, N. Niemeyer, and G. Traeger: "Laser and EB Welding of Magnesium Alloys," IIW Document No. IV-701-98, International Institute of Welding, July 1998.
10. M. Marya and G.R. Edwards: *Welding World (Int. Inst. Welding)*, 2000, vol. 44 (2), pp. 31-37.
11. T.W. Eagar and N.S. Tsai: *Welding J.*, 1983, vol. 62 (12), pp. 346s-355s.
12. T. Chande and J. Mazumder: *J. Appl. Phys.*, 1984, vol. 56, (7), pp. 1981-86.
13. J.C. Ion, H.R. Shercliff, and M.F. Ashby: *Acta Metall. Mater.*, 1992, vol. 40 (7), pp. 1539-51.
14. E.A. Metzbower: *J. Laser Appl.*, 1997, vol. 9 (1), pp. 23-33.
15. D. Rosenthal: *Trans. ASME*, 1946, vol. 68, pp. 849-65.
16. R.R. Rykalin: *Welding World*, 1974, vol. 12 (9–10), pp. 227-48.
17. C. Tix and G. Simon: *J. Phys. D: Appl. Phys.*, 1993, vol. 26 (11), pp. 2066-74.
18. J. Paulini, T. Klein, and G. Simon: *J. Phys. D: Appl. Phys.*, 1993, vol. 26 (6), pp. 1310-15.
19. A. Poueyo-Verwaerde, R. Fabbro, G. Deshors, A.M. de Frutos, and J. Orza: *J. Appl. Phys.*, 1993, vol. 74, pp. 5773-80.
20. Y. Arata, M. Tomie, N. Abe, and X.Y. Yao: *Trans. JWRI*, 1987, vol. 16, pp. 13-16.
21. E.A. Metzbower: *Metall. Mater. Trans. B*, 1996, vol. 26B, pp. 1029-33.
22. J. Kroos, U. Gratzke, M. Vicanek, and G. Simon: *J. Phys. D: Appl. Phys.*, 1993, vol. 26, pp. 481-86.
23. T. Klein, M. Vicanek, and G. Simon: *J. Phys. D: Appl. Phys.*, 1996, vol. 29, pp. 322-32.
24. S.J. Bless: IIW Document No. 2121-235-90, International Institute of Welding.
25. K. Mundra and T. Debroy: *Welding J.*, 1993, vol. 72 (1), pp. 1s-9s.
26. M. Collur, A. Paul, and J. Debroy: *Metall. Trans. B*, 1987, vol. 18B, pp. 733-40.
27. P. Burgardt and C.R. Heiple: *Welding J.*, 1992, vol. 71 (9), pp. 341s-346s.
28. M. Marya and S.K. Marya: *J. Mater. Eng. Performance*, 1998, vol. 7 (4), pp. 515-23.
29. M. Kuo, Z. Sun, and D. Pan: *Sci. Technol. Welding Joining*, 1998, vol. 3 (6), pp. 272-78.
30. A. Matsunawa, M. Seto, M. Mizutani, and S. Katayama: *Liquid Motion in Keyhole Laser Welding*, Laser Institute of America, American Institute of Physics, Laser Materials Processing, 1998, vol. 85, Part 2, pp. G151-G160.
31. A. Matsunawa, J.D. Kim, N. Seto, M. Mizutani, and S. Katayama: *J. Laser Appl.*, 1998, vol. 10 (6), pp. 247-54.
32. A.T D'Annessa: *Welding J.*, 1970, vol. 49 (2), pp. 41s-45s.
33. U. Gratzke, P.D. Kapadia, J. Dowden, J. Kroos, and G. Simon: *J. Phys. D: Appl. Phys.*, vol. 25, 1992, pp. 1640-47.